



Investigating the Evolution of Amati Parameters with Redshift

Meghendra Singh¹, Darshan Singh^{2,3}, Kanhaiya Lal Pandey⁴, Dinkar Verma² , and Shashikant Gupta²

¹ Delhi Metro Rail Corporation Limited, New Delhi 110001, India

² GD Goenka University, Gurugram 122103, India

³ Department of Physics, Mata Raj Kaur Institute of Engineering and Technology, Rewari 123401, India

⁴ Department of Physics, School of Advanced Sciences, Vellore Institute of Technology, Vellore 632014, India

Received 2023 April 2; revised 2023 October 24; accepted 2023 November 10; published 2024 January 9

Abstract

Gamma-ray bursts (GRBs) are among the brightest objects in the Universe and, hence, can be observed up to a very high redshift. Properly calibrated empirical correlations between intensity and spectral correlations of GRBs can be used to estimate the cosmological parameters. However, the possibility of the evolution of GRBs with redshift is a long-standing puzzle. In this work, we used 162 long-duration GRBs to determine whether GRBs below and above a certain redshift have different properties. The GRBs are split into two groups, and we fit the Amati relation for each group separately. Our findings demonstrate that estimations of the Amati parameters for the two groups are substantially dissimilar. We perform simulations to investigate whether the selection effects could cause the difference. Our analysis shows that the differences may be either intrinsic or due to systematic errors in the data, and the selection effects are not their true origin. However, in-depth analysis with a new data set comprised of 119 long GRBs shows that intrinsic scatter may partly be responsible for such effects.

Key words: Cosmology – gamma rays: general – (cosmology:) large-scale structure of universe – galaxies: high-redshift

1. Introduction

Gamma-ray bursts (GRBs), discovered in 1967 (Klebesadel et al. 1973), are the most powerful explosions in the Universe. The Compton Gamma Ray Observatory’s Burst and Transient Source Experiment (BATSE) confirmed the isotropic distribution of GRBs (Meegan et al. 1992; Pendleton et al. 1997), indicating that they are extragalactic. GRBs are short bursts of a gamma-ray flare which last from milliseconds to a few minutes. GRBs produce as much energy in a few seconds as the Sun does in its lifespan. Observations suggest two types of GRBs, short and long, based on T_{90} , the duration in which 90% of the burst energy is emitted. Short GRBs with $T_{90} < 2$ s are thought to result from compact star mergers. On the other hand, long GRBs are thought to arise from a massive star’s core collapse, with a length of $T_{90} > 2$ s (Woosley 1993; Paczyński 1998; MacFadyen & Woosley 1999; Kumar & Zhang 2015).

The ability to identify GRBs up to extremely high redshifts has long piqued the interest of cosmologists. Long GRBs provide a unique opportunity to investigate the properties of galaxies at high redshift, including galaxy evolution, star formation rate, and the intergalactic medium and interstellar medium (ISM) (Woosley & Bloom 2006; Dessauges-Zavadsky et al. 2008; Fynbo et al. 2009; Salvaterra et al. 2009; Tanvir et al. 2009; Cucchiara et al. 2011; Wang et al. 2015). In the last two decades, various relations between different observational parameters have been discovered, such as the Amati relation and Ghirlanda relation (Bloom et al. 2003; Ghirlanda et al. 2004;

Donaghy et al. 2005; Friedman & Bloom 2005; Firmani et al. 2006; Schaefer 2007). A recent study by Wang et al. (2022) utilized the X-ray plateau phases of long GRBs generated via dipole emission of magnetars revealing a tight correlation between the end time of plateau and the plateau luminosity. These relations have been used to calibrate secondary distance indicators.

The Amati relation is one of the most important relations in the context of GRBs. It is a correlation in the ν - F_ν spectrum between a GRB’s isotropic-equivalent energy (E_{iso}) and its intrinsic peak energy ($E_{\text{p,i}}$). It was discovered in 2002 (Amati et al. 2002), and subsequent research has confirmed it (Amati 2006; Amati et al. 2008, 2009). If the redshift, z , of the GRB is known, $E_{\text{p,i}}$ can be estimated from the observed peak energy, $E_{\text{p,obs}}$, using the relation

$$E_{\text{p,i}} = (1 + z)E_{\text{p,obs}}. \quad (1)$$

The Amati relation is then given by

$$E_{\text{p,i}} = K \left(\frac{E_{\text{iso}}}{10^{52} \text{ erg}} \right)^m, \quad (2)$$

where K and m are constants, and $E_{\text{p,i}}$ is expressed in keV. In Amati’s original study, m and K were determined to be $m \approx 0.5$ and $K \approx 95$, respectively (Amati et al. 2002). Later research using bigger samples of long GRBs supports the aforementioned range of K and m estimations. Alternatively, the Amati

relation can be expressed in the logarithmic form as

$$\log E_{\text{iso}} = a + b \log E_{\text{p},i}. \quad (3)$$

Equation (3) has the advantage of being linear. By taking logarithms on both sides, Equation (2) can be written as

$$\log E_{\text{iso}} = \frac{1}{m} \log E_{\text{p},i} - \frac{1}{m} \log K. \quad (4)$$

Comparing Equations (3) and (4), one can express a and b in terms of K and m as $a = -\frac{1}{m} \log K$ and $b = \frac{1}{m}$ respectively.

There are some issues with the Amati relation as well (Collazzi et al. 2012). One such issue is the redshift degeneracy in the $E_{\text{iso}}-E_{\text{peak}}$ relation (Li 2007a). Another problem is that approximately 48% of the GRBs in the BATSE data violate the Amati relation (Ehuad & Tsvi 2005). An improved Amati correlation has also been formulated (Liu et al. 2022b) which is in conflict with the standard Amati correlation (Liu et al. 2022a). It is also worth noting that hybrid samples with a wide range of redshifts are frequently used while fitting GRB data for correlations. As a result, the evolution of GRBs with redshift and the selection effects are often ignored.

It is counterintuitive to neglect the evolution of GRBs in the large redshift range $0.1 \leq z \leq 9$. Long-duration GRBs are more likely to occur in galaxies with low metallicity (Fynbo et al. 2003; Hjorth et al. 2003; Le Floch et al. 2003; Sollerman et al. 2005; Fruchter 2006). The isotropic energy of long GRBs is anti-correlated with the host galaxy's metallicity (Stanek et al. 2006). Metallicities are widely known to vary with cosmic redshift (Kewley & Kobulnicky 2005; Savaglio et al. 2005). According to Langer & Norman (2006), GRB evolution is expected as redshift increases. It makes sense to investigate the redshift dependence of the relations found in the GRB samples. Attempts to explore the redshift dependence of the Amati parameters have been made (Wang et al. 2011; Yan et al. 2021) wherein the authors found no, or marginal evolution of these parameters with redshift. Li (2007b) also investigated the redshift dependency of the Amati parameters, a and b , with the help of 48 long GRBs. These GRBs were divided into four redshift bins, and a linear variation in both a and b was observed. The authors claim that the variation could not be due to the selection effects. Dainotti et al. (2013) studied the origin of correlation between the X-ray luminosity (L_x) and the rest frame time (T_a). Dainotti et al. (2015) also investigated whether the redshift-dependent ratio of GRB rate to star formation evolves with redshift. Their results indicate a modest evolution of this ratio in the range $0.99 < z < 9.4$. The luminosity of host galaxies in the near-infrared (NIR) range is significantly high at redshifts below 1.5. Dust-obscured GRBs are mostly found in massive galaxies, but rarely in low-mass galaxies. This indicates that massive galaxies are mostly dusty, while low-mass galaxies contain little dust in their ISM. It is well known that the ratio of GRB rate to star formation is almost constant in metal-poor galaxies while it is suppressed in metal-rich

galaxies (Perley et al. 2016). This is linked to the GRB rate being low at $z < 1.5$. Tan & Wang (2015) studied the evolution of the luminosity function (LF) and the redshift selection effect of long GRBs. Their findings suggest that redshift detection efficiency, particularly in the range $1 < z < 2.5$, decreases with redshift giving rise to the redshift desert effect. It can be noted that the redshift desert is found in the case of low luminosity GRBs and the brighter GRBs have no contribution to it. In the present paper, we examine the evolution of the Amati parameters a and b with redshift. We also investigate whether the selection biases could be responsible for the possible redshift dependence if any. The data set used in our analysis contains three times more GRBs than Li (2007b). Various cosmological observations indicate quenching in galaxy clusters and a variation in star formation rate around a redshift of ~ 1.5 (Krumholz & Dekel 2012; Nantais et al. 2016; Ji et al. 2018; Bouwens et al. 2020). In light of the facts mentioned above, we plan to investigate the evolution of the Amati parameters, accordingly.

The rest of the paper is organized as follows: We outline the GRB data set and the analysis methods in Section 2. We offer a summary of our results and a brief explanation of the selection effect in Section 3 and present conclusions in Section 4.

2. Data and Methodology

2.1. Data

We require a data set that encompasses a large number of GRBs and spans a wide redshift range to study the evolution of GRBs. An updated compilation of long GRB data, which contains spectrum and intensity details as well as precise information about redshift, is available (Demianski et al. 2017). This data set contains 162 long GRBs and X-ray flashes with an extensive redshift range ($0.03 \leq z \leq 9.3$), making it suitable for our purpose. The major contribution in the data sample comes from the joint observations of Swift and Fermi or Konus-WIND; however, in some cases, $E_{\text{p},i}$ has been provided directly by the Swift/Burst Alert Telescope (BAT).

2.2. Methodology

To investigate the differences between GRB populations below and above the redshift, $z = 1.5$, we especially want to look at the development of the Amati parameters with redshift. Keeping in mind that the GRB production rate in galaxies differs below and above the redshift of 1.5 due to metallicity differences (Perley et al. 2016), we divide the GRB data into two groups of low and high redshift for this purpose. There are 71 GRBs in the low z sample, with a median redshift 0.86 and a range $0.033 < z < 1.489$. The high z sample consists of 91 GRBs with a redshift range $1.52 < z < 9.3$ and a median 2.48.

The isotropic-equivalent energy, E_{iso} , and peak energy, $E_{\text{p,i}}$, measurements, together with the observational errors, are known for the set of 162 GRBs. To fit for the Amati parameters a and b (see Equation (3)), one can define the χ^2 as follows

$$\chi^2 = \sum_{i=1}^N \left(\frac{g_i - f(E_{\text{p,i}}; a, b)}{\sigma_i} \right)^2, \quad (5)$$

where $g = \log E_{\text{iso}}$ is derived from data, and f is the theoretical value of $\log E_{\text{iso}}$ which can be computed using Equation (3). The Amati parameters a and b can be calculated by minimizing the χ^2 in Equation (5). The following analysis can be used to calculate σ_i of $\log E_{\text{iso}}$. The error in $\log E_{\text{iso}}$ due to observational uncertainty in E_{iso} is

$$dg = dE_{\text{iso}}/E_{\text{iso}}.$$

However, uncertainty in $\log E_{\text{iso}}$ depends on uncertainty in $\log E_{\text{p,i}}$, (see Equation (3))

$$df = b(dE_{\text{p,i}}/E_{\text{p,i}}).$$

Thus,

$$\sigma_i^2 = (dg)^2 + (df)^2 = (dE_{\text{iso}}/E_{\text{iso}})^2 + (b.(dE_{\text{p,i}}/E_{\text{p,i}}))^2. \quad (6)$$

The likelihood, $P(D|H)$, which is the probability of collecting data if the model H is correct, may be expressed in terms of χ^2 as follows

$$P(D|H(a, b)) \propto \exp(-\chi^2/2), \quad (7)$$

where χ^2 is defined by Equation (5). The parameters a and b can be estimated by maximizing likelihood with respect to these parameters. We employ the Bayesian methodology because the above-mentioned method does not provide a direct probability estimate for the Amati parameters. With the help of Bayes' theorem, the posterior probability of the Amati parameters can be calculated as

$$P(H(a, b)|D) \propto P(D|H(a, b)) \times P(H(a, b)). \quad (8)$$

The model's prior probability, $P(H)$, reflects our current understanding of the model. Because priors are subjective, careful consideration should be given to their selection. Another benefit of the Bayesian method is the marginalization of the nuisance parameters. For instance, marginalization over parameter a leads to the following equation

$$P(b|\mu) = \int P(\mu|a, b)P(a, b)da. \quad (9)$$

A similar procedure can be used to marginalize over the other parameter, b , as needed. To check if the Amati parameters evolve with redshift, we fit the Amati relation in Equation (3) for each subset using the methods discussed above.

2.3. Selection Biases

The selection effects in the prompt and afterglow observations may arise due to the sensitivity of the instrument as well

as the phenomena impacting the detection probability. Due to the instrument's sensitivity and the events that impact the detection likelihood, selection effects in the prompt emission and afterglow may develop. Some examples of instrumental biases (Coward et al. 2013) are the source localization from the telescope, and the source's position in the sky, especially if it is close to the Sun. Sometimes instrumental biases could be time-dependent, for instance, the learning curve of the instrument can affect the redshift distribution over time. The Malmquist bias arises due to the greater sensitivity of the instruments toward the brighter end of the LF. Knowledge of the LF is necessary to account for this bias.

Another important bias is the redshift desert which is related to the redshift measurement in the range $1.3 < z < 3$ (Coward et al. 2013). At a redshift of $z > 1$, the optical wavelength in the afterglow shifts to infrared. The sensitivity of a CCD drops in this region, and since signal to noise ratio is already poor for faint sources, it becomes difficult to measure the spectra.

The selection biases in the GRB data can lead to false positive results in our investigation. Hence, we perform simulations to test whether the selection biases impact our results. We first simulate a sample of z and E_{iso} following the distribution of the original data. Now, we produce $E_{\text{p,i}}$ by fitting the Amati relation to the above simulated sample. We put a lower limit $E_{\text{iso,lim}}$ on isotropic-equivalent energy in the simulation, keeping in mind the flux detection limit of the instruments. We divide the sample into low and high- z groups, as was done with the original data. Again, we fit the Amati relation to both groups. This exercise is repeated several times. Best-fit values of the Amati parameters are plotted, and a comparison between the low- z and high- z is made. One can repeat the exercise without implementing the lower limit $E_{\text{iso,lim}}$ on isotropic-equivalent energy. A comparison between the above two results infers whether the selection biases impact the earlier investigation result.

3. Results and Discussion

We first calculate the χ^2 and minimize it through the Amati parameters a and b . Minimum χ^2 per degree of freedom (dof) is found to be $\chi_r^2 = 6.32$. The large value of χ^2 per dof indicates that the errors in the data may have been underestimated. To obtain the direct probability of the parameters, we use the Bayesian approach through Equation (8). The best-fit values of the Amati parameters are presented in Table 1 along with their error bars. Figure 1(a) and (b) displays the posterior probability of each parameter. Bayesian marginalization on parameter b has been applied while calculating the posterior for a and vice-versa. For both parameters, uniform priors in a reasonable range have been considered.

The data are now divided into low- z and high- z groups, G_1 and G_2 , which contain 71 and 91 GRBs, respectively. Table 2 displays the details of these groups. As done previously, we

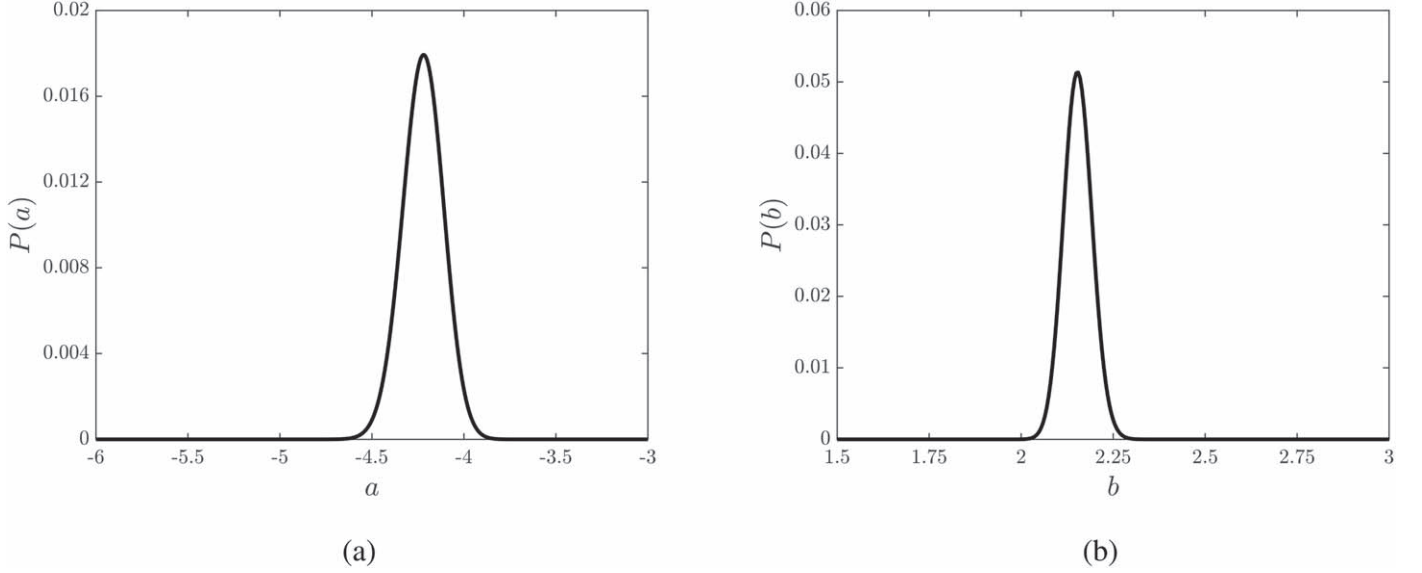


Figure 1. Posterior probability distribution for Amati parameters a , b for the set of 162 GRBs.

Table 1

Best-fit Values of the Amati Parameters, a and b , along with 1σ Confidence Level

a	b	σ_a	σ_b
-4.22	2.16	± 0.12	± 0.04

Note. The Bayesian approach has been applied to the complete set of 162 GRBs.

obtain the posterior probability of a and b for each group. Table 3 shows the best-fit values, while Figures 2 and 3 display the posterior probability distribution for each parameter. The distributions for the parameter a for the two groups, G_1 and G_2 , are different at around the 1.9σ level, as seen in Figure 2. The probability distributions for parameter b determined for the two groups are also different at more than the 2σ level, as demonstrated in Figure 3.

3.1. Analysis of Selection Effect

To confirm whether the differences in low and high redshift parameters are intrinsic, we need to analyze the selection effects which could be involved in the measurement process. Every detector has a lower detection limit of flux, hence the impact is that distant objects detected by the telescope would be intrinsically brighter. To investigate this impact, we use the following scheme, which is a modified version of Li (2007b).

First, we explore the distribution of the redshift, z , and isotropic-equivalent energy, E_{iso} , of the observed GRBs. They follow a log-normal distribution as depicted in Figure 4. The mean and standard deviation for $\log z$ are 0.18 and 0.34,

Table 2

Subgroups of GRBs

Group	Number of GRBs	Range of z	Median of z
G_1	71	0.033–1.489	0.86
G_2	91	1.52–9.3	2.48

Table 3

Best-fit Values of the Amati Parameters, a and b , along with the 1σ Errors for the Subgroups G_1 and G_2

Group	a	b
G_1	-3.79 ± 0.145	1.97 ± 0.06
G_2	-4.54 ± 0.240	2.26 ± 0.08

Note. The Bayesian approach has been used for the estimation.

respectively. The fit can be expressed as

$$f_1(\log z) = \frac{1}{\sqrt{2\pi}\sigma_1} \exp\left[-\frac{(\log z - \mu_1)^2}{2\sigma_1^2}\right]. \quad (10)$$

Similarly, the mean and standard deviation for $\log E_{\text{iso}}$ are 1.01 and 0.84, respectively, which can be expressed as

$$f_1(\log E_{\text{iso}}) = \frac{1}{\sqrt{2\pi}\sigma_2} \exp\left[-\frac{(\log E_{\text{iso}} - \mu_2)^2}{2\sigma_2^2}\right]. \quad (11)$$

Following (Li 2007b), we now simulate the GRB data to understand the selection effects. We generate 1000 sets of GRB samples, each containing 1000 values of z and E_{iso} using the

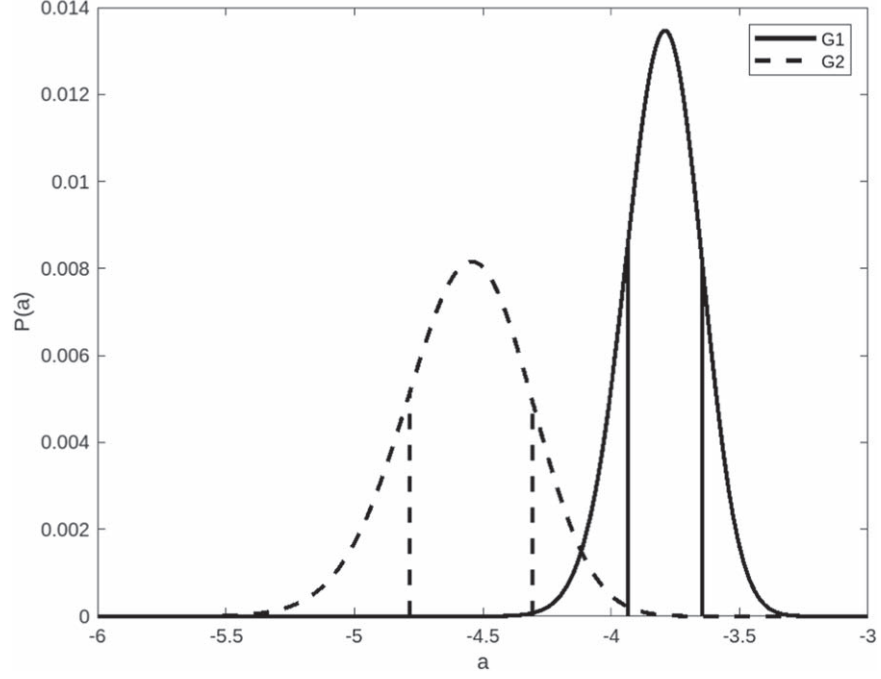


Figure 2. Posterior probability curve for the Amati parameter a for groups G_1 and G_2 . The values do not agree at 1.9σ .

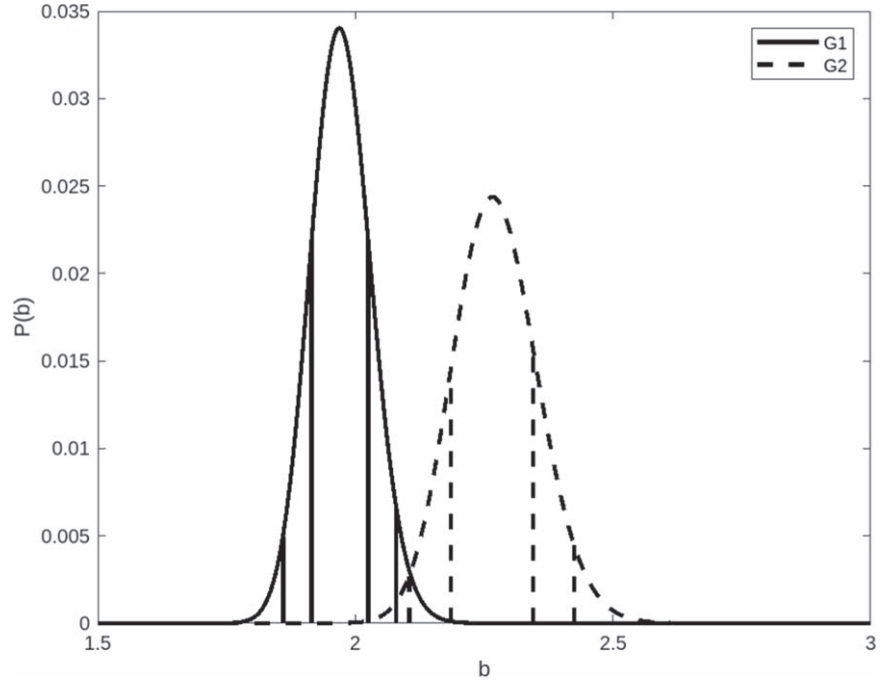


Figure 3. Posterior probability curve for the Amati parameter b for groups G_1 and G_2 . The values do not agree at the 2σ level.

log-normal distribution of Equations (10) and (11), respectively. The distribution's mean and standard deviation are the same as those of the observed GRBs in Figure 4. Keeping in mind that every detector has a lower flux detection limit, we put

a lower limit of E_{iso} in the simulated data. In Figure 5, we plot the isotropic-equivalent energy of the 162 GRBs in our sample. The plot clearly affirms that the (observed minimum) isotropic energy is correlated with the redshift. The solid line in the plot

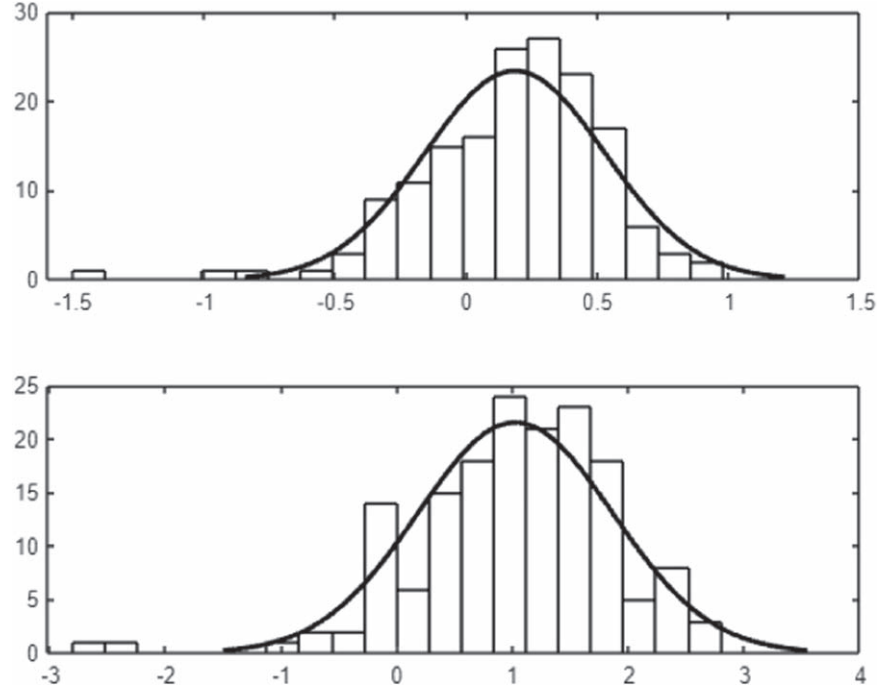


Figure 4. Distribution of redshift, z , and isotropic-equivalent energy, E_{iso} , of the observed long GRBs. The $\log z$ values in the data fit a log-normal distribution with a mean 0.18 and standard deviation 0.34 (upper panel). $\log E_{\text{iso}}$ values also fit a log-normal distribution with mean 1.01 and standard deviation 0.84 (lower panel).

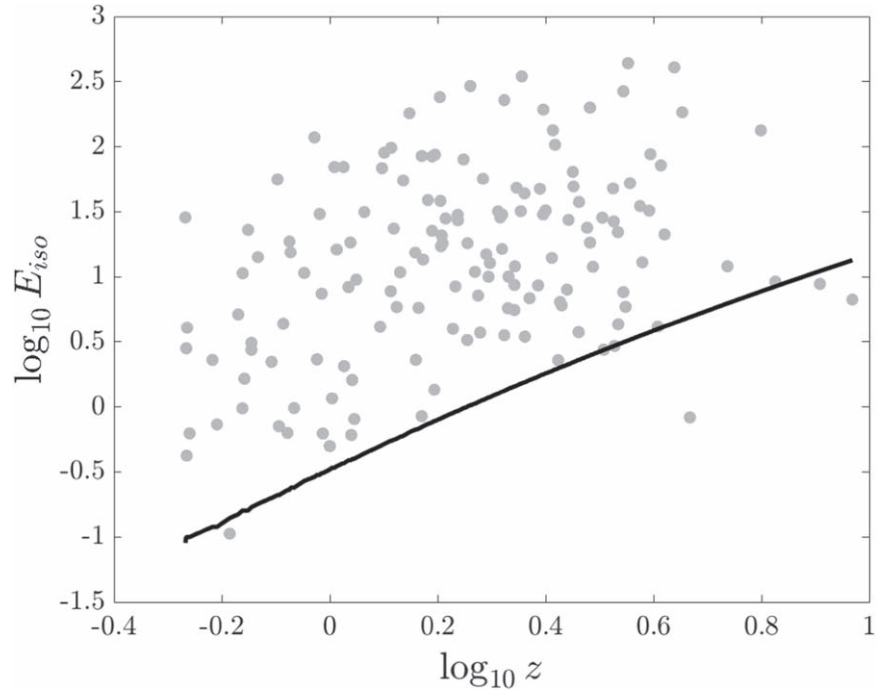


Figure 5. Variation of isotropic-equivalent energy (E_{iso}) with redshift (z) of 162 GRBs. The solid line has been plotted using Equation (12) with a bolometric fluence limit of $F_{\text{bol,lim}} = 10^{-9} \text{ erg cm}^{-2}$. The solid line shifts upward when $F_{\text{bol,lim}}$ is increased.

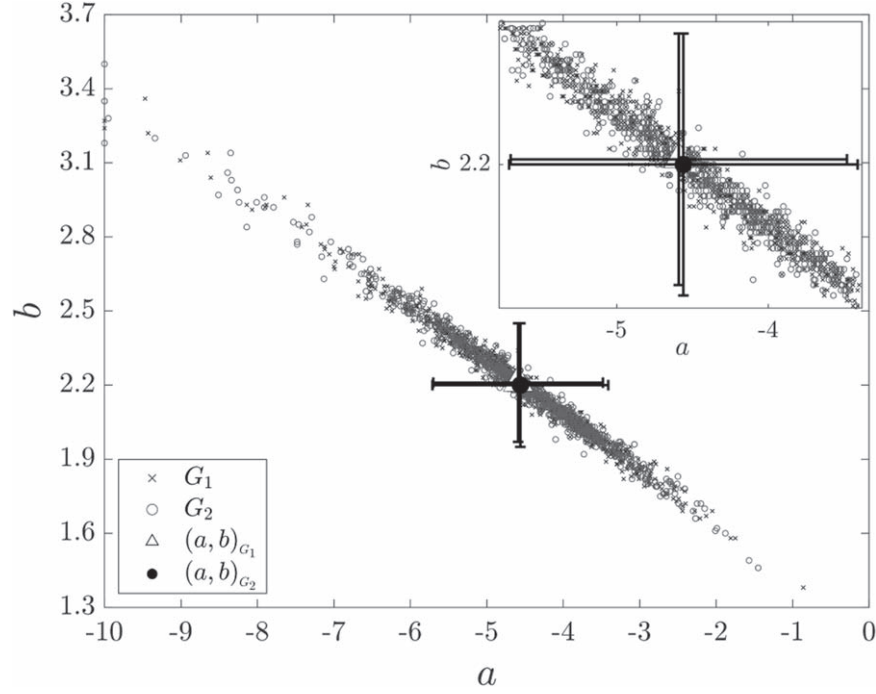


Figure 6. Best-fit values of the Amati parameters, a and b , for simulated data sets. Each data set consists of 1000 values of z and E_{iso} which are further divided into low and high- z groups (G_1 and G_2). A lower limit on E_{iso} has been imposed using Equation (12). Symbol “.” represents simulated data sets for low- z while “x” signifies high- z simulated data sets. Empty and dark circles show the average best-fit values of a and b from the low- z and high- z groups of simulated data respectively.

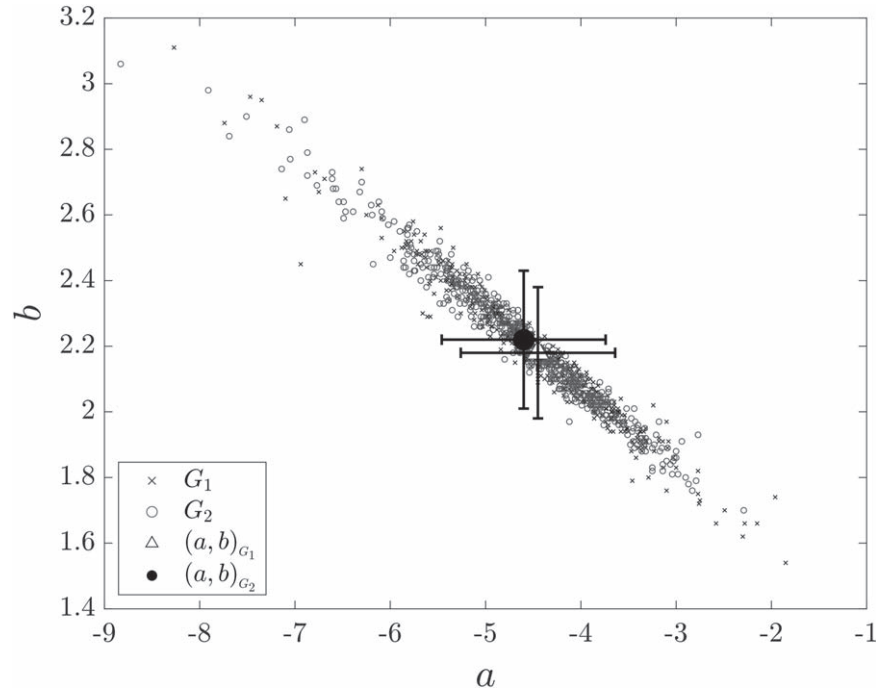


Figure 7. Best-fit values of the Amati parameters, a and b , for simulated data sets. No lower limit has been imposed on E_{iso} . Symbol “.” represents simulated data sets for low- z while “x” signifies high- z simulated data sets. Empty and dark circles show the average best-fit values of a and b from the low- z and high- z groups of simulated data respectively.

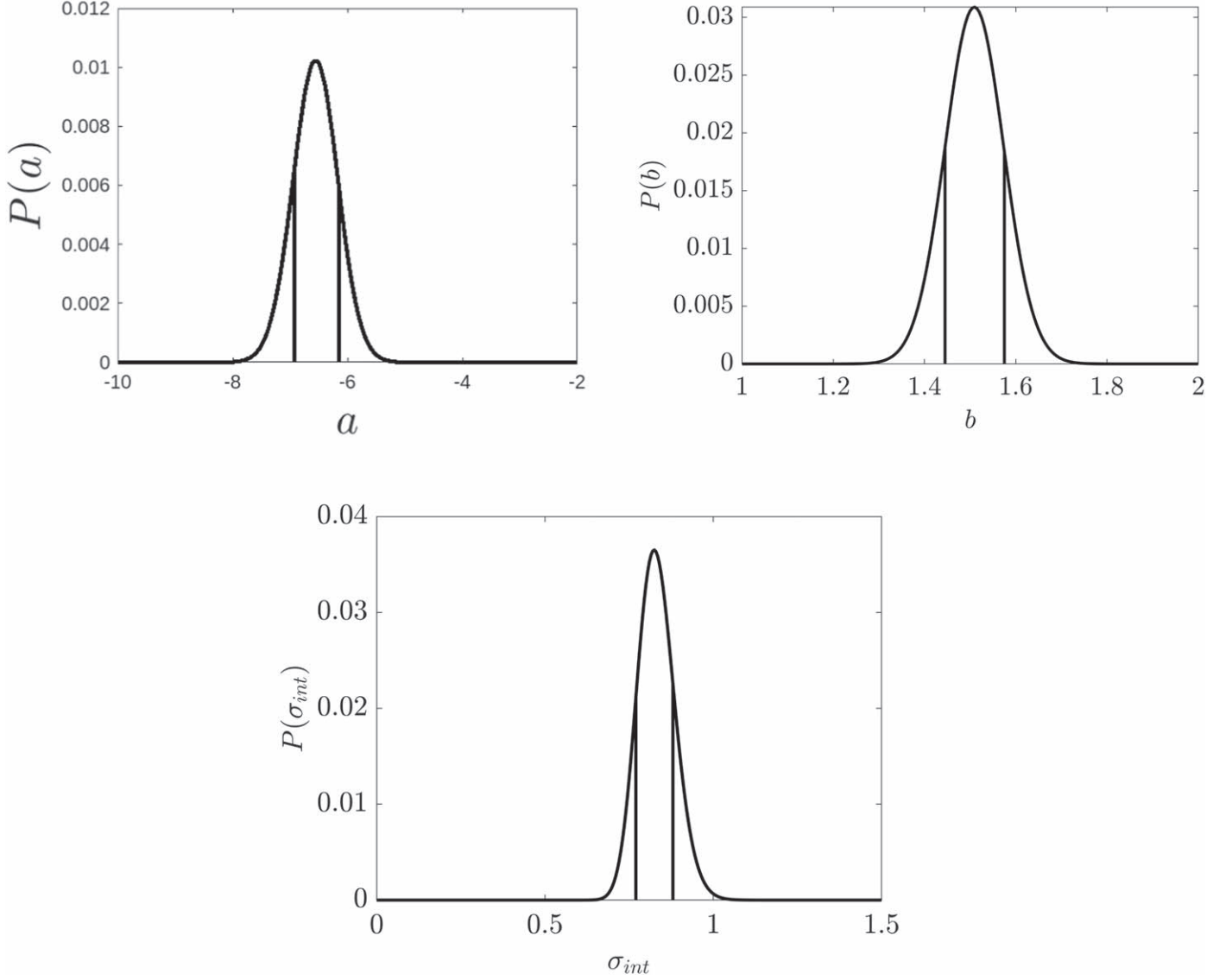


Figure 8. Posterior probability distribution for Amati parameters a , b and σ_{int} for the set of 162 GRBs.

shows the limit corresponding to a typical value for the bolometric fluence, $F_{\text{bol,lim}} = 10^{-9} \text{ erg cm}^{-2}$, which fairly represents the lower limit of the isotropic-equivalent energy of a detectable burst at redshift z in our sample. At the redshift z , the lower limit on E_{iso} can be given as

$$E_{\text{iso,lim}} = 4\pi D_{\text{com}}^2 (1 + z) F_{\text{bol,lim}}, \quad (12)$$

where D_{com} is the comoving distance to the burst. Having the set of (z, E_{iso}) pairs, we generate $E_{\text{p,i}}$ for each pair as

$$f_2(y) = \frac{1}{\sqrt{2\pi} \sigma_3} \exp \left[-\frac{(y - sx - p)^2}{2\sigma_3^2} \right], \quad (13)$$

Table 4

Best-fit Values of the Amati Parameters a, b along with 1σ Confidence Level

Data Set	a	b	σ_{int}
162	-6.54 ± 0.39	1.51 ± 0.06	0.83 ± 0.05
G_1	-6.77 ± 0.51	1.52 ± 0.09	0.87 ± 0.09
G_2	-5.19 ± 0.71	1.32 ± 0.11	0.77 ± 0.07

Note. The Bayesian approach has been applied in all cases.

where $x = \log(E_{\text{iso}})$ and $y = \log(E_{\text{p,i}})$. Here, s and p represent the slope and intercept for the relation, $y = sx + p$. Having the sample of $(z, E_{\text{iso}}, E_{\text{p,i}})$, we divide them into low and high- z groups with the boundary as $z = 1.5$. Now, we determine the

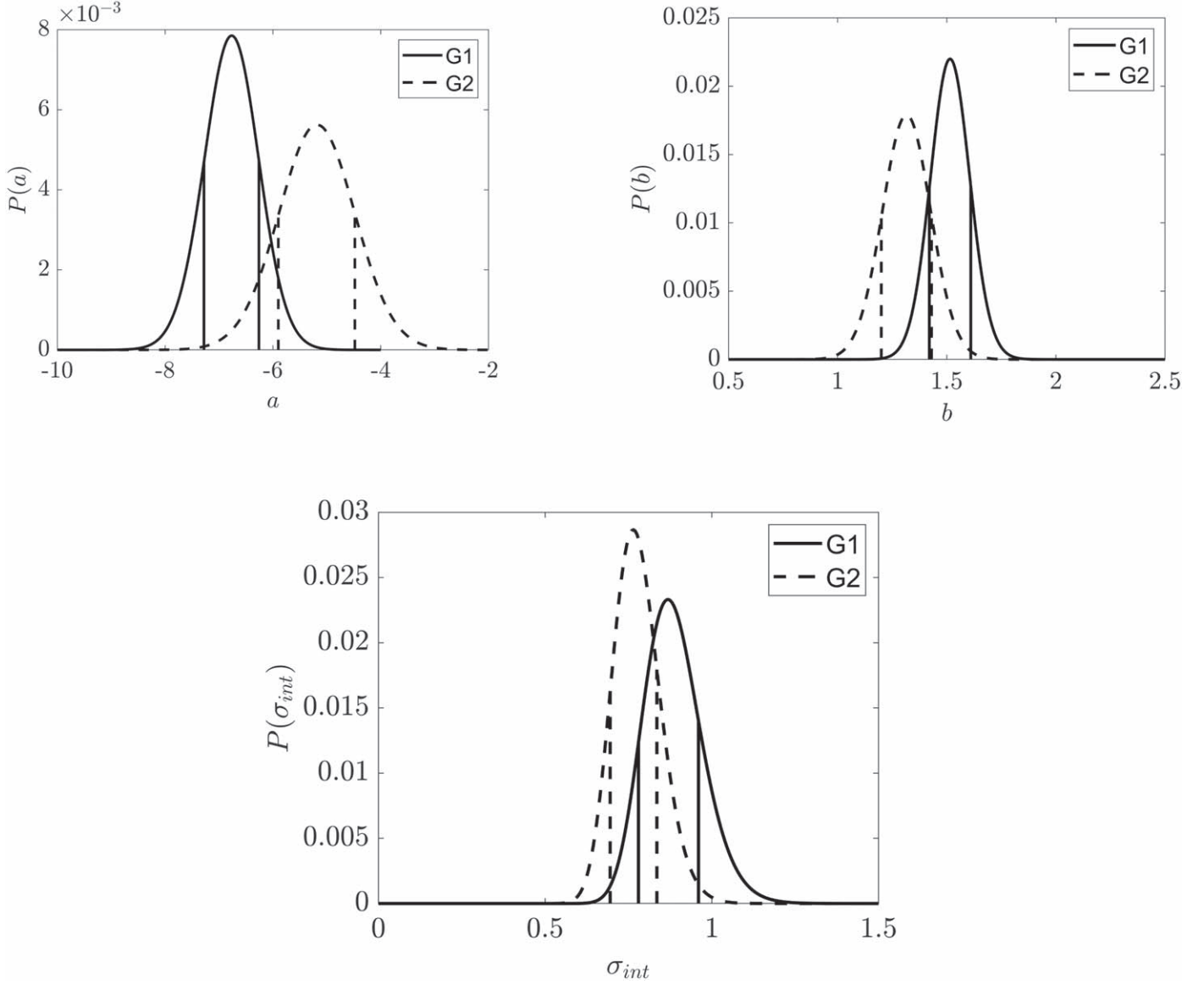


Figure 9. Posterior probability distribution for Amati parameters a , b and σ_{int} for two groups for the set of 162 GRBs.

Table 5

Best-fit Values of the Amati Parameters a , b along with 1σ Confidence Level

Data Set	a	b	σ_{int}
119	-3.30 ± 0.59	1.04 ± 0.10	1.03 ± 0.07
G_1	-3.00 ± 1.17	0.88 ± 0.19	1.27 ± 0.19
G_2	-3.75 ± 0.70	1.09 ± 0.11	0.90 ± 0.08

Note. The Bayesian approach has been applied in all cases.

Amati parameters for both groups in the sample. This process is repeated one thousand times, and the distribution of the Amati parameters for these samples is displayed in Figure 6. The graph shows that most of the best-fit values of the two groups

overlap. In fact, the average value of the Amati parameters for the low redshift group is $(-4.59, 2.21)$ and that for the high redshift group is $(-4.56, 2.20)$, which do not differ much from each other. This conflicts with Figures 2 and 3 indicating that the 2σ difference in Amati parameters for low and high- z samples is not expected. To explore the matter further, we turn off the lower limit on E_{iso} , defined in Equation (12), and again simulate one thousand samples of z and E_{iso} , each containing 1000 data points. Similar to the preceding instance, Equation (13) is used to generate $E_{p,i}$ corresponding to each pair of z and E_{iso} . Each sample is again divided into low and high- z groups, and best-fit is obtained. The best-fit values have been plotted in Figure 7. Similar to Figure 6, most of the values

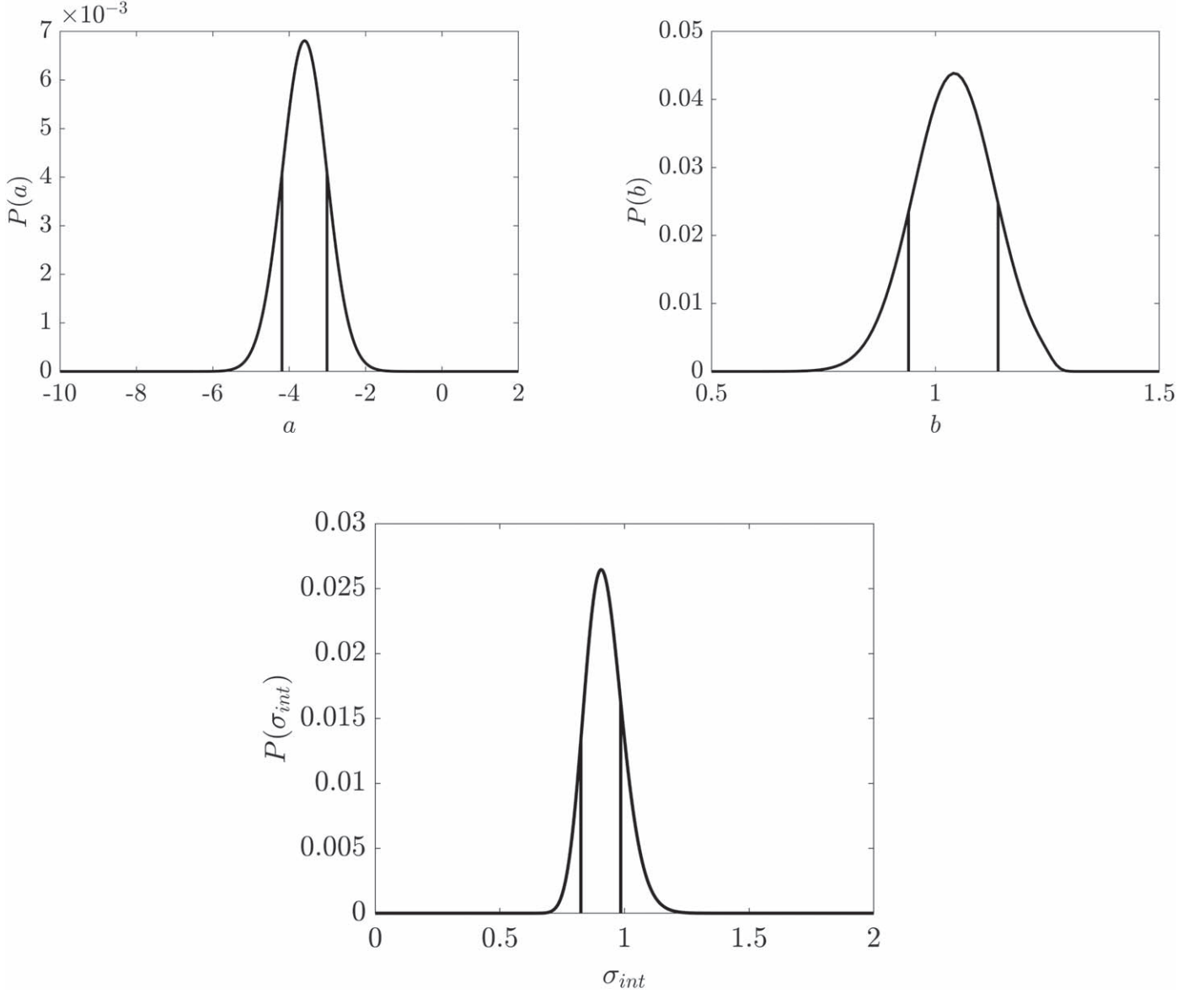


Figure 10. Posterior probability distribution for Amati parameters a , b and σ_{int} for the set of 119 GRBs.

overlap, and there is hardly any difference in the average values of the Amati parameters for low and high- z groups.

3.2. Intrinsic Scatter

The intrinsic scatter affects the Amati relation and should be taken into account. A different likelihood function, also known as the Reichart's likelihood function (Reichart et al. 2001), is used for this purpose. It takes scatter (σ_{int}) into account in addition to the linear relation represented by Equation (3) and is

given as

$$L_{\text{Reichart}}(a, b, \sigma_{\text{int}}) = \frac{1}{2} \frac{\sum \log(\sigma_{\text{int}}^2 + \sigma_{y_i}^2 + a^2 \sigma_{x_i}^2)}{\log(1 + a^2)} + \frac{1}{2} \sum \frac{(y_i - ax_i - b)^2}{\sigma_{\text{int}}^2 + \sigma_{x_i}^2 + a^2 \sigma_{x_i}^2}, \quad (14)$$

which is now a three-parameter function. One can fit all three parameters simultaneously. Alternatively, it is also possible to evaluate the b parameter analytically by setting

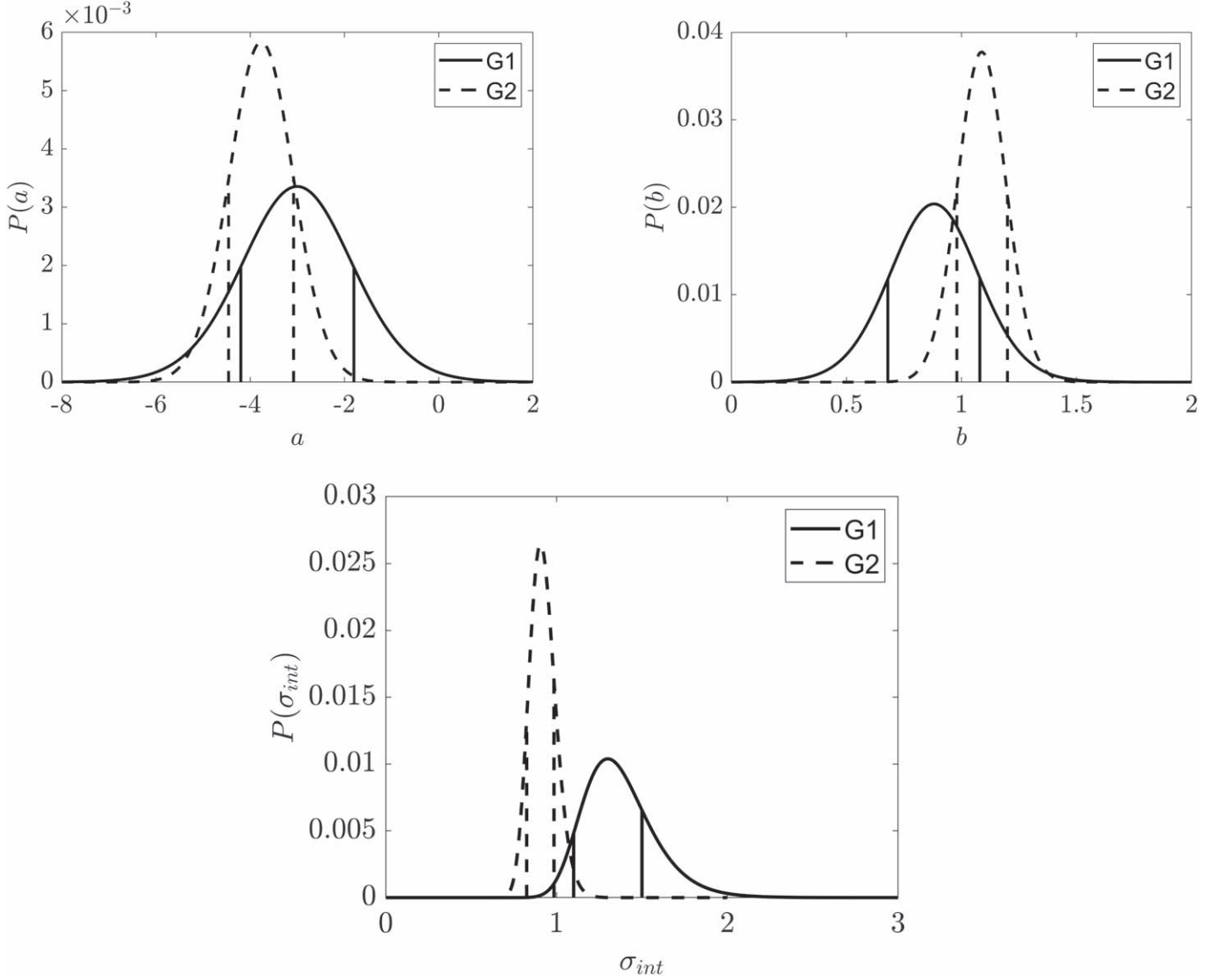


Figure 11. Posterior probability distribution for Amati parameters a , b and σ_{int} for two groups for the set of 119 GRBs.

$\frac{\partial}{\partial b} L(a, b, \sigma_{\text{int}}) = 0$. We obtain

$$b = \left[\sum \frac{y_i - ax_i}{\sigma_{\text{int}}^2 + \sigma_{y_i}^2 + a^2 \sigma_{x_i}^2} \right] \left[\sum \frac{1}{\sigma_{\text{int}}^2 + \sigma_{y_i}^2 + a^2 \sigma_{x_i}^2} \right]^{-1}. \quad (15)$$

In order to understand the effect of intrinsic scatter, we obtain the best-fit values of parameters a , b and σ_{int} simultaneously using the above three-parameter likelihood function defined by Equation (14). However, while calculating the best-fit value of one parameter, Bayesian marginalization has been applied on the other two parameters. Row one of Table 4 shows the best fit

values of these parameters along with the 1σ uncertainty. The values are clearly different from the two-parameter likelihood fit. Now, we separately fit these parameters for the two groups, G_1 and G_2 . The best-fit values of a for these groups are shown in the same Table 4. The posterior probability distributions of parameters a , b and σ_{int} for the full data set are depicted in Figure 8. The vertical lines represent the 1σ region. The same for groups G_1 and G_2 are displayed in Figure 9. In case of parameter a , the two groups still disagree at more than the 1σ level. For parameter b , the two groups barely overlap at the 1σ level. However, both the groups clearly overlap for σ_{int} . Thus we conclude that (i) the intrinsic scatter affects the best-fit value

of Amati parameters, however, (ii) for both parameters a and b , introduction of intrinsic scatter in the likelihood reduces the discrepancy for the groups G_1 and G_2 .

3.3. Comparison with Other GRB Data Sets

To understand if there could be other systematic issues present in the data, we also work with a different data set. It consists of 119 GRBs observed through Fermi-LAT which is the combination of 25 GRB measurements from Dirirsa et al. (2019) over the redshift range of $0.3399 \leq z \leq 4.35$, given in Table 2 of Dirirsa et al. (2019), and 94 GRB measurements from Wang et al. (2016) over the redshift range $0.48 \leq z \leq 8.2$, given in Table 5 of Dirirsa et al. (2019). One should note that this data set does not contain the very low redshift ($z < 0.3$) GRBs. We repeat the analysis for Amati parameters a , b and σ_{int} using the three-parameter likelihood function for this relatively new GRB data set. As in the previous case, these data are also divided into two subsets with a cutoff at $z = 1.5$. The best fit values of the full data set as well as those of the two subsets are shown in Table 5. Clearly, the best fit values are quite different from those obtained from the 162 GRB data. The values of a and b for the two subsets also match within the error bars. However, the best-fit values of σ_{int} for the two subsets do not agree with each other. The distributions of posterior probability are displayed in Figures 10 and 11. The possible reasons for the difference between the behavior of the two data sets could be the (i) small number of low- z GRBs in the 119 data, or/and (ii) the presence of systematic effects in any one of the two sets.

4. Conclusion

The goal of the present work was to study the possible redshift evolution of the Amati relation, which is a correlation between the isotropic-equivalent energy, E_{iso} , and the peak energy, $E_{\text{p},i}$. If the GRB properties evolve with redshift, it will be reflected in the Amati parameters. Alternatively, the selection biases could also lead to false detection of the evolution. We have applied the Bayesian approach to estimate the Amati parameters a and b along with the intrinsic scatter, σ_{int} . The data set containing 162 long GRBs up to a redshift of 9.3 (Demianski et al. 2017) was divided into two groups below and above redshift $z = 1.5$. The selection of $z \sim 1.5$ is appropriate as the quenching activity in galaxy clusters and a change in star formation rate have been indicated around this redshift (Krumholz & Dekel 2012; Nantais et al. 2016; Ji et al. 2018; Bouwens et al. 2020). Our analysis in Section 3 shows that when the intrinsic scatter is not taken into account, the best-fit values of Amati parameters for the two groups of GRBs are quite different. The values do not match at the $\sim 2\sigma$ level. In order to determine whether the disparity in our analysis may be caused by the presence of selection biases, we simulate the GRB data. Our analysis ruled out the selection bias as the

possible cause of the mismatch. At first sight, it seems reasonable to infer that the mismatch in the low and high- z values of the Amati parameters could be linked with the evolution of GRB with redshift, and in line with recent studies (Lloyd-Ronning et al. 2019; Dainotti et al. 2021a) which suggest a strong evolution of parameters like E_{iso} , T_{90} and GRB luminosity. However, we have performed additional analyses to test the robustness of our results. The first of these is related to the intrinsic scatter. We show in Section 3.2 that, although the values of Amati parameters a and b change when the intrinsic scatter is considered, however, the low and high redshift GRBs still disagree at around the 1σ level. The second constraint is implemented by comparing the analysis of 162 GRB data to that of a more recent data set. When a similar analysis is performed on a recent data set containing 119 GRBs, the discrepancy in the parameters a and b between low- z and high- z GRBs disappears. This suggests that either one of these or both of the data sets may contain systematic errors. Thus, acceptance or rejection of the evolution hypothesis necessitates additional analysis with more recent data sets and the application of additional techniques, which we plan to accomplish in our future work.

There have been several attempts to constrain cosmological parameters using GRB data. The resulting constraints are significantly weaker, however, consistent with the constraints coming from the baryon acoustic oscillations (BAO) and $H(z)$ data (Khadka & Ratra 2020; Khadka et al. 2021). Alternatively, the evolution of parameters of the standard cosmological model has also been studied (Dainotti et al. 2021b; Colgáin et al. 2022a, 2022b; Jia et al. 2023). Understanding the possible evolution might be beneficial in the calibration of GRBs as secondary distance indicators. This has the potential to change our understanding of high-redshift cosmology.

Acknowledgments

M.S. thanks DMRC for support. D.S. thanks the compeers of GD Goenka University for continuing assistance.

ORCID iDs

Dinkar Verma  <https://orcid.org/0000-0002-8744-5891>
Shashikant Gupta  <https://orcid.org/0000-0003-2923-9245>

References

- Amati, L. 2006, *MNRAS*, **372**, 233
- Amati, L., Frontera, F., Tavani, M., et al. 2002, *A&A*, **390**, 81
- Amati, L., Guidorzi, C., Frontera, F., et al. 2008, *MNRAS*, **391**, 577
- Amati, L., Frontera, F., & Guidorzi, C. 2009, *A&A*, **508**, 173
- Bloom, J. S., Frail, D. A., & Kulkarni, S. R. 2003, *ApJ*, **594**, 674
- Bouwens, R., González-López, J., Aravena, M., et al. 2020, *ApJ*, **902**, 112
- Colgáin, E. Ó., Sheikh-Jabbari, M. M., Solomon, R., Dainotti, M. G., & Stojkovic, D. 2022a, arXiv:2206.11447
- Colgáin, E. Ó., Sheikh-Jabbari, M. M., Solomon, R., et al. 2022b, arXiv:2203.10558

- Collazzi, A. C., Schaefer, B. E., Goldstein, A., & Preece, R. D. 2012, [ApJ](#), **747**, 39
- Coward, D. M., Howell, E. J., Branchesi, M., et al. 2013, [MNRAS](#), **432**, 2141
- Cucchiara, A., Levan, A. J., Fox, D. B., et al. 2011, [ApJ](#), **736**, 7
- Dainotti, M., Levine, D., Fraija, N., & Chandra, P. 2021a, [Galaxies](#), **9**, 95
- Dainotti, M. G., Petrosian, V., Singal, J., & Ostrowski, M. 2013, [ApJ](#), **774**, 157
- Dainotti, M. G., Simone, B. D., Schiavone, T., et al. 2021b, [ApJ](#), **912**, 150
- Dainotti, M. G., Vecchio, R. D., Shigehiro, N., & Capozziello, S. 2015, [ApJ](#), **800**, 31
- Demianski, M., Piedipalumbo, E., Sawant, D., & Amati, L. 2017, [A&A](#), **598**, A112
- Dessauges-Zavadsky, M., Prochaska, J. X., & Chen, H.-W. 2008, Probing the Interstellar Medium and Stellar Environments of Long-Duration GRBs, Massive Stars as Cosmic Engines (Cambridge: Cambridge Univ. Press), 457, Proceedings of the International Astronomical Union
- Dirisa, F. F., et al. 2019, [ApJ](#), **887**, 13
- Donaghy, T. Q., Graziani, C., & Lamb, D. Q. 2005, [NCimC](#), **28**, 403
- Ehudad, N., & Tsvi, P. 2005, [MNRAS](#), **360**, L73
- Firmani, C., Avila-Reese, V., Ghisellini, G., & Ghirlanda, G. 2006, [MNRAS](#), **372**, L28
- Friedman, A. S., & Bloom, J. S. 2005, [ApJ](#), **627**, 1
- Fruchter, A. S. 2006, [Natur](#), **441**, 463
- Fynbo, J. P. U., Jakobsson, P., Møller, P., et al. 2003, [A&A](#), **406**, L63
- Fynbo, J. P. U., Jakobsson, P., Prochaska, J. X., et al. 2009, [ApJS](#), **185**, 526
- Ghirlanda, G., Ghisellini, G., Lazzati, D., & Firmani, C. 2004, [ApJL](#), **613**, L13
- Hjorth, J., et al. 2003, [ApJ](#), **597**, 699
- Ji, Z., Giavalisco, M., Williams, C. C., et al. 2018, [ApJ](#), **862**, 135
- Jia, X. D., Hu, J. P., & Wang, F. Y. 2023, [A&A](#), **674**, A45
- Kewley, L., & Kobulnicky, H. A. 2005, Metallicity of Star-Forming Galaxies, in Starbursts, ed. R. de Grijs & R. M. Gonzalez Delgado (Dordrecht: Springer), 307
- Khadka, N., Luongo, O., Muccino, M., & Ratra, B. 2021, [JCAP](#), **2021**, 042
- Khadka, N., & Ratra, B. 2020, [MNRAS](#), **499**, 391
- Klebesadel, R. W., Strong, I. B., & Olson, R. A. 1973, [ApJL](#), **182**, L85
- Krumholz, M. R., & Dekel, A. 2012, [ApJ](#), **753**, 16
- Kumar, P., & Zhang, B. 2015, [PhR](#), **561**, 1
- Langer, N., & Norman, C. A. 2006, [ApJL](#), **638**, L63
- Le Floc'h, E., Duc, P.-A., Mirabel, I. F., et al. 2003, [A&A](#), **400**, 499
- Li, L.-X. 2007a, [MNRAS](#), **374**, L20
- Li, L.-X. 2007b, [MNRAS: Letters](#), **379**, L55
- Liu, Y., Chen, F., Liang, N., et al. 2022a, [ApJ](#), **931**, 50
- Liu, Y., Liang, N., Xie, X., et al. 2022b, [ApJ](#), **935**, 7
- Lloyd-Ronning, N. M., Aykutaalp, A., & Johnson, J. L. 2019, [MNRAS](#), **488**, 5823
- MacFadyen, A. I., & Woosley, S. E. 1999, [ApJ](#), **524**, 262
- Meegan, C. A., Fishman, G. J., Wilson, R. B., et al. 1992, [Natur](#), **355**, 143
- Nantais, J. B., van der Burg, R. F. J., Lidman, C., et al. 2016, [A&A](#), **592**, A161
- Paczynski, B. 1998, [ApJL](#), **494**, L45
- Pendleton, G. N., Paciesas, W. S., Briggs, M. S., et al. 1997, [ApJ](#), **489**, 175
- Perley, D. A., et al. 2016, [ApJ](#), **817**, 7
- Reichart, D. E., Lamb, D. Q., Fenimore, E. E., et al. 2001, [ApJ](#), **552**, 57
- Salvaterra, R., Della Valle, M., Campana, S., et al. 2009, [Natur](#), **461**, 1258
- Savaglio, S., Glazebrook, K., Le Borgne, D., et al. 2005, [ApJ](#), **635**, 260
- Schaefer, B. 2007, [ApJ](#), **660**, 16
- Sollerman, J., Östlin, G., Fynbo, J. P. U., et al. 2005, [NewA](#), **11**, 103
- Stanek, K. Z., et al. 2006, [AcA](#), **56**, 333
- Tan, W.-W., & Wang, F. Y. 2015, [MNRAS](#), **454**, 1785
- Tanvir, N. R., Fox, D. B., Levan, A. J., et al. 2009, [Natur](#), **461**, 1254
- Wang, F., Dai, Z., & Liang, E. 2015, [NewAR](#), **67**, 17
- Wang, F. Y., Hu, J. P., Zhang, G. Q., & Dai, Z. G. 2022, [ApJ](#), **924**, 97
- Wang, F.-Y., Qi, S., & Dai, Z.-G. 2011, [MNRAS](#), **415**, 3423
- Wang, J. S., Wang, F. Y., Cheng, K. S., & Dai, Z. G. 2016, [A&A](#), **585**, A68
- Woosley, S. E. 1993, [ApJ](#), **405**, 273
- Woosley, S. E., & Bloom, J. S. 2006, [ARA&A](#), **44**, 507
- Yan, D., Xiao-Gang, Z., Zheng-Xiang, L., He, G., & Zong-Hong, Z. 2021, [A&A](#), **651**, L8